remote sensing

MDPI

Article

The Impact of the Mesoscale Ocean Variability on the Estimation of Tidal Harmonic Constants Based on Satellite Altimeter Data in the South China Sea

Qian Yu [1], Haidong Pan [2], Yanqiu Gao [3,4,*] and Xianqing Lv [1]

[1] Qingdao Collaborative Innovation Center of Marine Science and Technology (CIMST), Physical Oceanography Laboratory, Ocean University of China, Qingdao 266100, China; yuqian@stu.ouc.edu.cn (Q.Y.); xqinglv@ouc.edu.cn (X.L.)
[2] Laboratory of Marine Science and Numerical Modeling, First Institute of Oceanography, Ministry of Natural Resources, Qingdao 266061, China; panhaidong@stu.ouc.edu.cn
[3] State Key Laboratory of Satellite Ocean Environment Dynamics, Second Institute of Oceanography, Ministry of Natural Resources, Hangzhou 310012, China
[4] Southern Marine Science and Engineering Guangdong Laboratory, Zhuhai 519082, China
* Correspondence: gaoyanqiu@sio.org.cn

Abstract: The estimation accuracy of tidal harmonic constants is of great significance to maritime traffic and port construction. However, due to the long sampling period of satellite altimeters, tidal signals alias the mesoscale ocean frequencies. As a result, the harmonic analysis is affected by mesoscale environmental noise. In this study, the influence of the mesoscale ocean variability (MOV) on the estimation of tidal harmonic constants was quantified by analyzing 25 years of altimeter data from the Topex/Poseidon (T/P) and Jason satellites in the South China Sea (SCS). The results indicated that the absolute amplitude differences (AADs) of the eight major tidal constituents before and after the mesoscale variability correction (MVC) were generally within 10 mm, and most were within 6 mm. For the relative impact, M_2, O_1, and K_1 were not obviously affected by the MOV because of their large amplitudes, and the AADs generally accounted for less than ±10% of the amplitudes. As a tidal constituent with amplitude less than 2 cm in the SCS, the amplitude of K_2 was significantly affected by the MOV, with the ratios of the AADs to its own amplitudes ranging from −64.79% to 95.99% in space. In terms of phase, the K_2 tide was most affected by the MOV: 63% of the data points before and after correction were over ±5°, and the maximum and minimum values were 86.46° and −176.27°, respectively. The absolute phase differences of other tidal constituents before and after the MVC were generally concentrated within ±5°. The impact of the MOV on the evolution of tidal amplitudes in the SCS was also explored. It was found that the MOV can cause pseudo-rapid temporal variations of tidal amplitudes in some regions of the SCS.

Keywords: tides; tidal harmonic analysis; satellite altimeter data; mesoscale variability

Citation: Yu, Q.; Pan, H.; Gao, Y.; Lv, X. The Impact of the Mesoscale Ocean Variability on the Estimation of Tidal Harmonic Constants Based on Satellite Altimeter Data in the South China Sea. *Remote Sens.* **2021**, *13*, 2736. https://doi.org/10.3390/rs13142736

Academic Editors: Angelo Perilli, Mariona Claret and Alexandre Stegner

Received: 6 May 2021
Accepted: 8 July 2021
Published: 12 July 2021

1. Introduction

Tides, one of the most prevalent ocean motions, are the periodic movements of sea water induced by the celestial tide-generating force from the sun and the moon. Previous studies have shown that ocean tides have important effects on earth rotation, ocean circulation, deep ocean mixing, etc. [1,2]. The accuracy of ocean tides estimation plays an important role in numerous fields, such as coastal engineering, maritime traffic, and aquaculture [3].

Until the 1990s, ocean tidal data were obtained mainly from tide gauges around the world. Due to the limitation of location and quantity, water level records were mainly observed in coastal areas, and few tidal gauges were located in the deep sea. The advent and wide use of satellite altimetry have revolutionized the ocean observation scale in space. However, there are also limitations to this technique. Because the tidal signals

of the Topex/Poseidon and Jason (T/P-Jason) satellites are sampled over a period of 9.915642 days, the semidiurnal and diurnal tides are aliased into low-frequency fluctuations with periods of several months. Desai et al. (1997) and Tierney et al. (1998) found that mesoscale energy in the ocean reduced the accuracy of tidal estimation due to the long sampling interval, which can be alleviated by increasing the time series of satellite altimeters [4,5]. At present, although the satellite data have a long time span, the nontidal background noise still affects the accuracy of tidal harmonic constants to some extent, especially in the regions with strong mesoscale ocean variability (MOV). Ray and Byrne (2010) analyzed tidal features in the southeast Atlantic Ocean using bottom pressure records collected at 11 stations aligned on a single ground track of the T/P-Jason satellites. By comparing the estimated tidal constants, they found that high MOV clearly corrupted the altimeter-based tidal estimations even with data spanning a 17 year period. They further used a multi-satellite mapped sea level anomalies (SLA) product as a "correction" for tide estimation, thus improving the accuracy of the altimeter-based harmonic constants [6].

MOV mainly exists in the form of mesoscale eddies, which are the horizontal rotating water in the ocean with a horizontal diameter of 100~500 km and a duration of several days to several months. Mesoscale eddies are an important component of dynamical oceanography across the range of scales. They can transport heat, mass momentum, and biogeochemical properties from one area to other, remote areas [7].

As the largest semi-enclosed marginal sea in the western Pacific, the South China Sea (SCS) has attracted oceanographers because of its significant monsoon climate, special geographical location, and rich natural resources. Since 1956, mesoscale eddies have been discovered in the South China Sea [8]. Previous studies have shown that the SCS is a region with one of the strongest MOVs in the world and the upper layer of the SCS has complex structural characteristics [9,10]. Since the launch of the Topex/Poseidon satellite in 1992, numerous studies on tidal characteristics in the SCS have been performed [11–14]. However, it appears that no studies have discussed in detail the potential influence of MOV on tidal estimation in the SCS. One of the purposes of this paper is to fill this gap.

In this study, the mesoscale variability correction (MVC) method proposed by Ray and Byrne (2010) was applied to the SCS, and the newest harmonic tidal analysis package S_TIDE [15] (add see the Supplementary Materials) was used to conduct tidal analysis on the T/P-Jason data. The paper is organized as follows. Section 2 describes the satellite altimeter data for tidal harmonic analysis and the multi-satellite mapped sea level anomaly (SLA) fields for MVC. The influence of MOV on the extraction of tidal amplitudes and phases is analyzed in Section 3. An improved understanding of tidal evolution from satellite altimeter data using the MVC method is discussed in Section 4. Section 5 presents the conclusion and summary.

2. Data and Methods

2.1. Altimetric Data

The sea level observations for tidal harmonic analysis were taken from four satellite altimeters: Topex/Poseidon (T/P) and three Jason satellites (Jason-1, Jason-2, and Jason-3). The orbital period of these satellites is 112.0 min, and the repetition period is 9.915642 days. To ensure consistency, the system bias caused by different terrestrial reference frames was removed and the four altimeter datasets were combined. In this study, the observations with a total length of 25 years from October 1992 to September 2017 were analyzed. To ensure the accuracy and the reliability of this research, we selected 1600 observation points with a time span longer than 18.61 years and missing values less than 20%. It can be seen that the selected points are mainly concentrated in the central deep-sea basin of the SCS (Figure 1).

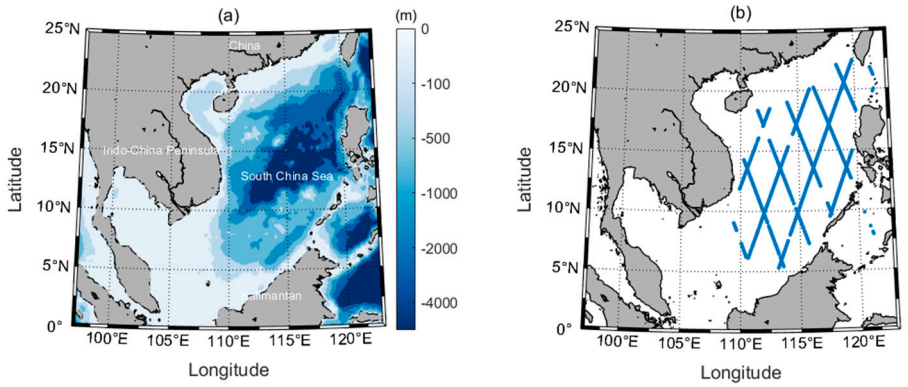

Figure 1. (**a**) The depth map and (**b**) the map of selected T/P-Jason satellite observation points in the South China Sea.

Similar to the approach of Ray and Byrne (2010) [6], multi-satellite gridded daily SLA fields provided by the Copernicus Marine and Environment Monitoring Service (CMEMS) were used for MVC. This SLA product merges all available altimeter missions (T/P-Jason, ENVISAT, Geosat Follow-On (GFO), AltiKa, Haiyang-2A, etc.) [16]. The filter method introduced by Zaron and Ray (2018) was used to eliminate the residual tidal signals in this mapped SLA product, and the remaining information was identified as the mesoscale variability. By subtracting the filtered SLA fields from the T/P-Jason data, the influence of the MOV on satellite-based tidal estimation was removed and the MOV operation was completed [17].

2.2. Tidal Aliasing in Altimetric Data

As mentioned above, tidal aliasing refers to a phenomenon during the sampling process in which, due to the long sampling interval, the component with a frequency higher than the folding frequency in the original time series folds towards that with a low frequency, thus, forming false spectral lines (peaks) in the frequency spectrum and causing confusion between the high and low frequency components [18]. According to the sampling theory, when the sampling interval is determined, the highest frequency that can be resolved is the folding frequency. Because the sampling period of T/P-Jason satellites is 9.915642 days, the oscillation period that can be identified is about 20 days. Because tides are mainly composed of diurnal and semidiurnal tides, the tidal signals with high frequency are folded into signals with low frequency. The minimum period corresponding to the folding frequency is the aliasing period (Table 1).

Table 1. The periods and aliasing periods of major tidal constituents under the T/P-Jason sampling interval.

Constituent	Tidal Period (h)	Aliasing Period (Days)
M_2	12.42	62.1
S_2	12.00	58.7
K_1	23.93	173.2
O_1	25.82	45.7
N_2	12.66	49.5
K_2	11.97	86.6
P_1	24.07	88.9
Q_1	26.87	69.4

It should be noted that the mesoscale eddies (with periods ranging from ten days to half a year) are common in the SCS. Chen et al. (2011) conducted a statistical analysis of the mesoscale eddies in the SCS using 17 years of satellite data from October 1992 to October 2009, in which a total of 393 cyclonic eddies and 434 anticyclonic eddies were

extracted, and the average lifetime of these eddies was 8.8 weeks (61.6 days) [10]. The own periods and aliasing periods of major tidal constituents under the T/P-Jason sampling interval are shown in Table 1 [19]. It can be seen that the aliasing period of main tidal constituents is close to the mean period of mesoscale eddies. Thus, the results of harmonic analysis of satellite altimeter data include two parts: ocean tide (barotropic tide and the surface manifestation of internal tide) and MOV. In the SCS, due to the high mesoscale eddy activities, the tidal harmonic constants are disturbed by MOV, and the accuracy of tidal estimation is partly limited.

According to the Rayleigh criterion, the length of record (LOR) required to separate the two different tidal constituents should satisfy the following:

$$\left|\frac{1}{T_i}-\frac{1}{T_j}\right|T' \geq 1, \text{ which is } T' \geq \left|\frac{T_iT_j}{T_i-T_j}\right|. \tag{1}$$

Thus, the LOR required to separate the eight main tidal constituents in T/P-Jason observations can be obtained (Table 2). The LOR to fully separate P_1 and K_2 is 9.18 years, which is the longest compared to other pairs of constituents. The period of 9.18 years is significantly less than the 25 years of altimeter data recorded in this paper. Therefore, the eight major constituents can be guaranteed to be fully resolved.

Table 2. Time spans for 8 major tidal constituents to be fully separated (unit: year).

Constituent	M_2	S_2	K_1	O_1	N_2	K_2	P_1	Q_1
M_2	–	2.97	0.27	0.47	0.67	0.60	0.56	1.63
S_2		–	0.24	0.56	0.86	0.50	0.47	1.05
K_1			–	0.17	0.19	0.47	0.50	0.32
O_1				–	1.63	0.27	0.26	0.37
N_2					–	0.32	0.31	0.47
K_2						–	9.18	0.95
P_1							–	0.86
Q_1								–

2.3. Tidal Harmonic Analysis

The observed sea level h can be regarded as the superposition of n tidal constituents. Equation (3) is the linearized version of Equation (2).

$$h = h_0 + \sum_{i=1}^{n} f_i H_i \cos(\omega_i t + u_i - g_i) \tag{2}$$

$$h = h_0 + \sum_{i=1}^{n} f_i [U_i \cos(\omega_i t + u_i) + V_i \sin(\omega_i t + u_i)] \tag{3}$$

where H_i and g_i are the amplitude and the phase of the tidal constituents, respectively, which are collectively called harmonic constants. h_0 is the mean sea level. ω_i, f_i, and u_i are the frequency, the nodal factor, and the nodal angle of i-th constituent, respectively. U_i and V_i are transformed by:

$$\begin{aligned} U_i &= H_i \cos g_i \\ V_i &= H_i \sin g_i \end{aligned} \tag{4}$$

When conducting linear regression, Equation (3) is converted to the following matrix form:

$$H = AX \tag{5}$$

where H, A, and X are the matrix of observed sea levels, the matrix of known coefficients, and the matrix of the parameters that need to be solved, respectively. When there are m sea level observations, the matrices are expressed as follows:

$$H = \begin{pmatrix} H(t_1) & H(t_2) & \cdots & H(t_m) \end{pmatrix}^T \tag{6}$$

$$\mathrm{X} = \begin{pmatrix} h_0 & U_1 & \cdots & U_n & V_1 & \cdots & V_n \end{pmatrix}^T \tag{7}$$

$$A = \begin{pmatrix} 1 & F(1,1) & \cdots & F(n,1) & G(1,1) & \cdots & G(n,1) \\ 1 & F(1,2) & \cdots & F(n,2) & G(1,2) & \cdots & G(n,2) \\ \cdots & \cdots & \cdots & \cdots & \cdots & \cdots & \cdots \\ 1 & F(1,m) & \cdots & F(n,m) & G(1,m) & \cdots & G(n,m) \end{pmatrix} \tag{8}$$

where $F(i,j) = f_i(t_j)\cos(\omega_i t_j + u_i(t_j))$ and $G(i,j) = f_i(t_j)\sin(\omega_i t_j + u_i(t_j))$.

Unknown tidal parameters can be estimated using Equation (9):

$$\mathrm{X} = \left(A^T A\right)^{-1} A^T H \tag{9}$$

To eliminate the effects of some outliers in tidal signals, iteratively reweighed least squares (IRLS) regression, which is the extension of the ordinary least squares (OLS), was performed in this study. Previous study [20,21] showed that the IRLS algorithm can reduce the influence of broad-spectrum noise and thus improve the reliability of the regression results. The newest harmonic tidal analysis package, S_TIDE, was used in this study to realize the IRLS algorithm [22].

Before evaluating the results of the tidal harmonic analysis, we first verify the reliability of the regression results using the signal-to-noise ratio (SNR), which can be described by:

$$\mathrm{SNR} = \left(\frac{H}{H_e}\right)^2 \tag{10}$$

where H is the estimated amplitude of a tidal constituent and H_e is the estimated error [23]. In general, the SNR can analyze the characteristics and influence of nontidal components on tidal estimation in the course of harmonic analysis. A higher SNR indicates a lower noise level in the tidal signal and, thus, the harmonic constants will be more reliable [24].

Table 3 shows the space-averaged changes of SNR for the eight major tidal constituents before and after the MVC. We find that the errors of tidal amplitudes can be obviously reduced and the corresponding SNRs are significantly increased after the MVC, which represents a significant improvement in the accuracy and reliability of the estimated tidal constants. Among all the SNRs of the eight main constituents, that of K_2 constituent is the smallest. The amplitudes of K_2 are the smallest among the eight main tides in the SCS, which means that K_2 tides are more vulnerable to the influence of MOV. On the contrary, the SNRs of M_2, O_1, and K_1 constituents are larger than the others, indicating that the amplitudes of these constituents are less affected by the nontidal components. These three tidal constituents are the most important constituents in the SCS, and their large amplitudes weaken the influence of background noises.

Previous statistical analyses have shown that the mesoscale eddies are concentrated in the west of the Luzon Strait and the western boundary of the deep-sea basin. They are also distributed in the south of the north slope of the SCS and the middle of the deep-sea basin [25–28]. The errors of M_2 and S_2 error in the western Luzon Strait and the western boundary of the deep-sea basin (framed areas in Figure 2a) are larger than those in other regions, which is consistent with the significant area of mesoscale eddies in the SCS. Lower SNRs are also found in these regions (Figure 3). The phenomenon is clearly mitigated, although did not disappear completely after MOV. Other tides also conform to this distribution.

Table 3. Comparison of the space-averaged error and SNR of eight main tidal constituents before and after the MVC in the South China Sea.

Constituent	Error before Correction (mm)	Error after Correction (mm)	SNR before Correction	SNR after Correction
M_2	8.89	5.82	336.98	787.45
S_2	8.95	5.87	47.25	108.93
K_1	9.09	5.96	1114.32	2581.42
O_1	9.07	5.95	844.69	1963.79
N_2	8.89	5.82	14.35	33.04
K_2	8.99	5.89	4.39	10.26
P_1	8.96	5.87	113.07	263.48
Q_1	9.04	5.92	31.79	73.81

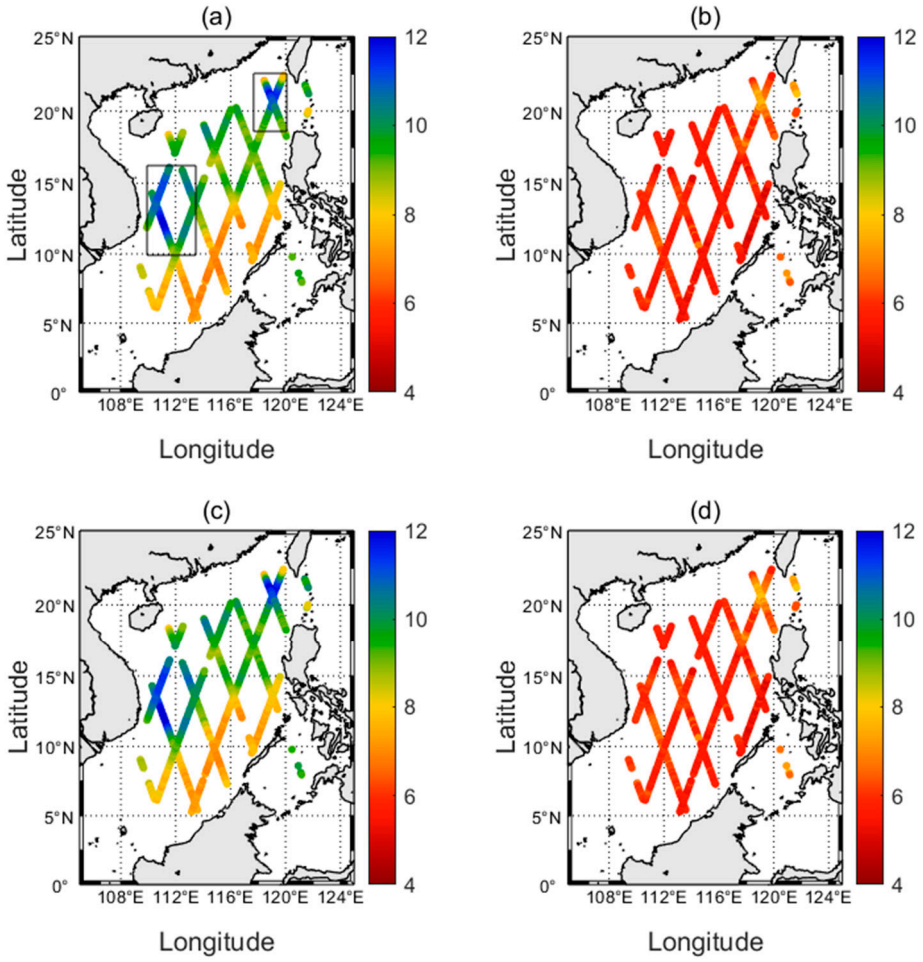

Figure 2. Comparison of estimated error (mm) of M_2 and O_1 constituents before and after the MVC: (**a**) error of M_2 constituent before correction; (**b**) error of M_2 constituent after correction; (**c**) error of O_1 constituent before correction; (**d**) error of O_1 constituent after correction.

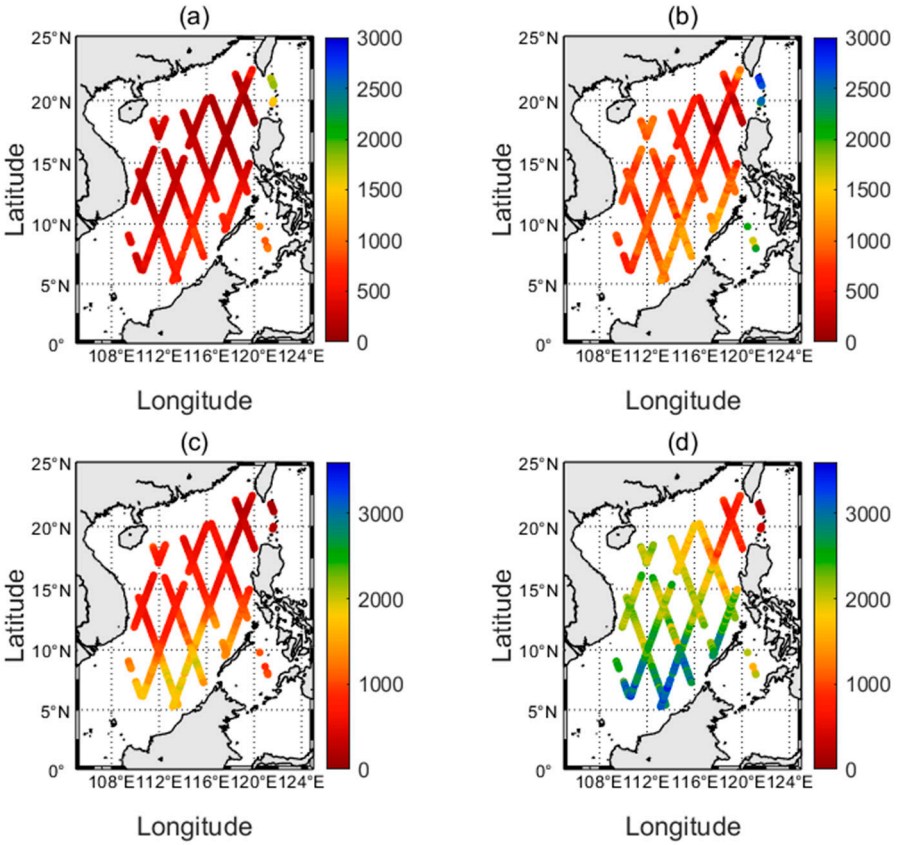

Figure 3. Spatial distribution of SNR of M_2 and O_1 constituents: (**a**) SNR of M_2 constituent before correction; (**b**) SNR of M_2 constituent after correction; (**c**) SNR of O_1 constituent before correction; (**d**) SNR of O_1 constituent after correction.

3. Results

3.1. The Effect of MVC on the Estimation of Tidal Amplitude

Figure 4 shows the results of the amplitude difference (ΔH) before and after MVC (detailed distribution statistics are displayed in Table A1 in Appendix A). The distributions of the amplitude differences of eight major constituents conforms to a Gaussian distribution whose mathematical expectation is nearly zero, which indicates that, for most data points, the MOV has negligible effects on the results of the tidal harmonic analysis. The potential effects of the MOV should only be considered at a small number of points at which the MOV is strong. It was found that the influence of MOV has different effects on the estimation of the amplitudes of the eight main tides, although they are all mainly distributed within ±10 mm and most of them are concentrated within ±6 mm. The amplitude differences of N_2 tides are small: the maximum and minimum amplitude differences are 8.4 and −8.3 mm, respectively. At about 64.81% of the total data points, the amplitude differences of N_2 tides are between ±2 mm. The amplitude differences of K_1 and M_2 are the largest among the eight main constituents: at about only 35.56% (46.38%) of the data points, the amplitude differences of K_1 (M_2) are between ±2 mm, and at 22.31% (9.44%) of the data points, the amplitude differences of K_1 (M_2) are beyond ±6 mm, with a maximum value of 16.2 (15.2) mm and a minimum value of −16.8 (−17.9) mm.

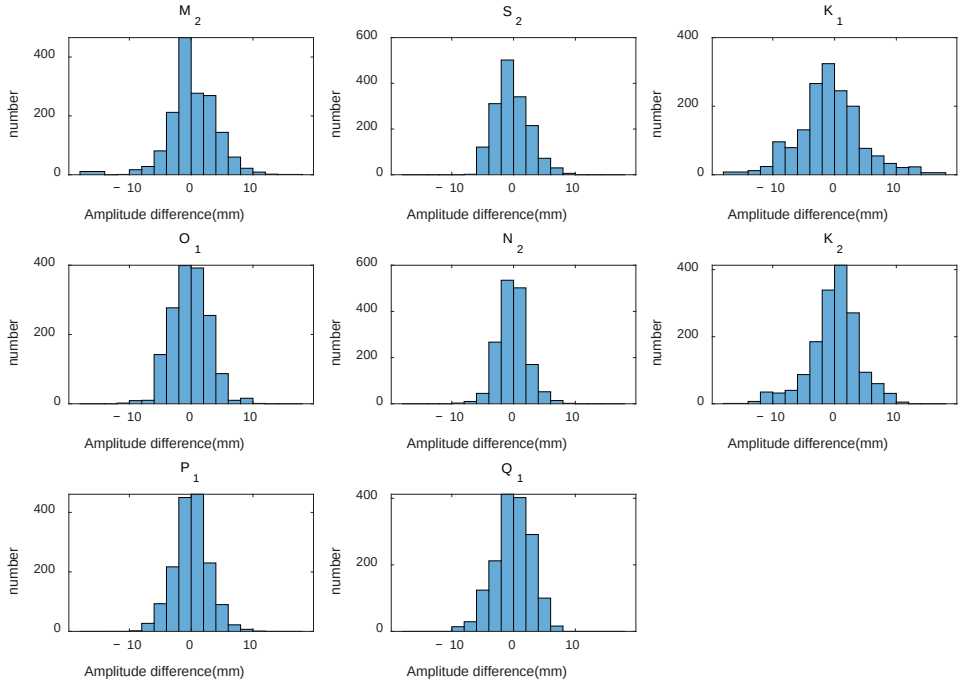

Figure 4. Histogram of amplitude differences (mm) before and after the MVC for eight major tides in the South China Sea.

Considering the fact that the eight major constituents have different magnitudes in amplitudes, the ratio ($\Delta H/H$) of amplitude differences before and after MVC (ΔH) to the amplitude after correction (H) were derived, and this ratio was defined as the relative influence of the MOV on tidal estimation. Table 4 shows the maximum and minimum values of the relative influence acting on each tidal constituent. As the most important tidal constituents in the SCS, M_2, O_1, and K_1 tides have average amplitudes of tens of centimeters, which can help to weaken the relative impact of the MOVs on themselves in the case of the same magnitude of amplitude difference. For example, in the case of the O_1 tide, which benefits from a large amplitude, the relative influence of the MOV ranges from −3.12% to 5.59%, which is the least among all the tidal constituents. The extreme values of relative influence on the M_2 (K_1) tide are 12.97% (9.13%) and −7.43% (13.36%), respectively. The amplitude estimates of these three tidal constituents are least affected by the MOV in terms of the relative influence. As the tide with amplitudes of a few centimeters, the K_2 tide has the maximum (95.99%) and minimum (−64.79%) ratio of amplitude difference to the average amplitude, indicating that the amplitude estimation of K_2 tide is the most relatively affected by the MOV.

Table 4. The extreme ratio of amplitude difference to the corrected amplitude of the eight major tides in the South China Sea. H_1 and H_2 are the corrected amplitudes.

Constituent	H_1 (mm)	ΔH_{max} (mm)	$\Delta H_{max}/H_1$ (%)	H_2	ΔH_{min} (mm)	$\Delta H_{min}/H_2$ (%)
M_2	116.9	15.2	12.97	139.2	−10.3	−7.43
S_2	33.0	6.0	18.16	33.4	−4.9	−14.65
K_1	177.5	16.2	9.13	95.3	−12.7	−13.36
O_1	185.9	10.4	5.59	320.9	−10.0	−3.12
N_2	19.0	6.7	35.24	35.3	−8.2	−23.22
K_2	11.9	11.4	95.99	20.8	−13.5	−64.79
P_1	80.0	11.0	13.78	36.1	−4.3	−11.88
Q_1	36.1	6.4	17.74	23.6	−5.7	−24.29

To further demonstrate the effect of MVC, we introduced the global ocean tidal model TPXO9 and FES2014 [29]. The TPXO9 tidal model was developed based on the Oregon State University Tidal Inversion Software (OTIS) and assimilates a large number of satellite altimetry data and tidal gauge observations. It is generally believed that, although the tidal constants provided by the TPXO9 model still have some room for improvement in coastal areas with complex topography and coastlines, the prediction of this model is extremely close to the actual values in the deep ocean [30]. The FES2014 is the newest global ocean tidal atlas, and aims to provide altimetry data with tidal de-aliasing correction. Due to the unstructured grid flexible resolution, recent progress in hydrodynamic tidal solutions, and use of the ensemble data assimilation technique, the FES2014 atlas shows extremely significant improvements in all ocean compartments, and particularly in shelf and coastal seas [31]. The effect of MVC can be evaluated by comparing the results of TPXO9 and the FES2014 with those of harmonic analysis of T/P-Jason data.

The estimated tidal amplitudes on selected points at which the altimeter-based tidal estimates are most seriously affected by MOV are compared with those based on TPXO9 and FES2014 (Tables 5 and 6), and the locations of the selected points are shown in Figure 5. At most selected data points, altimeter-based tidal estimates are closer to the TPXO9 (FES2014) model after MVC. For example, the error rate of Q_1 tidal amplitude at 20.45°N, 119.00°E sharply decreases from 20.8% (18.6%) to 3.73% (1.1%). At 109.99°E and 12.08°N, the error rate of N_2 tidal amplitude sharply decreases from −30.93% (−26.0%) to −6.01% (−2.0%).

In general, the minor tidal constituents can be deduced by major constituents, which are called tidal inference. Inference is also used in satellite altimeter analyses when a constituent cannot be well determined due to either noise or aliasing problems [32]. The standard ratio routinely used in tidal inference calculations for P_1 to K_1 is 0.3309 and for K_2 to M_2 is 0.1270 according to the equilibrium tidal theory [33–35]. After accounting for the nearby diurnal free wobble (NDFW) resonance, P_1/K_1 is expected to be approximately 0.3180 [36]. Figure 6 is a histogram of P_1/K_1 and K_2/M_2 in the SCS. Obviously, both before and after correction, the peaks are all close to their standard ratio, but in the corrected histograms, the results cluster more closely to the standard ratio.

Table 5. Altimeter-based tidal estimates at selected points.

Number	Constituent	Location (Lon, Lat)	Amplitude before Correction (mm)	Amplitude after Correction (mm)
1	M_2	(119.5127, 19.5467)	101.8	116.9
2	M_2	(115.7900, 19.5617)	148.8	142.0
3	S_2	(118.7611, 21.3209)	40	47.4
4	S_2	(117.9117, 16.5196)	38.3	33.4
5	K_1	(118.7081, 19.7563)	161.3	177.5
6	K_1	(121.6240, 19.9540)	108.1	95.3
7	O_1	(118.9299, 20.9271)	175.5	185.9
8	O_1	(110.0481, 7.3512)	330.9	320.9
9	N_2	(119.2644, 20.1387)	12.3	19
10	N_2	(109.9920, 12.0775)	43.6	35.3
11	K_2	(115.4216, 18.6728)	0.5	11.9
12	K_2	(110.7611, 13.0509)	34.7	21.2
13	P_1	(115.9345, 19.9070)	69.0	80.0
14	P_1	(121.6033, 19.9047)	40.4	36.1
15	Q_1	(118.9988, 20.4466)	29.7	36.1
16	Q_1	(121.6240, 19.9540)	29.4	23.6

Table 6. The tidal amplitudes from TPXO9 and FES2014 models at selected points.

Number	TPXO9			FES2014		
	Amplitude from Model (mm)	The Error Rate before Correction (%)	The Error Rate after Correction (%)	Amplitude from Model (mm)	The Error Rate before Correction (%)	The Error Rate after Correction (%)
1	126.3	19.4	7.4	133.9	24.0	12.7
2	139.6	−6.6	−1.7	141.3	−5.3	−0.5
3	60.9	34.3	22.2	65.5	38.9	27.6
4	34.3	−11.7	2.6	36.9	−3.8	9.5
5	207.2	22.2	14.3	207.0	22.1	14.3
6	83.7	−29.2	−13.9	104.6	−3.3	8.9
7	186.1	5.7	0.1	183.7	4.5	−1.2
8	316.0	−4.7	−1.6	316.1	−4.7	−1.5
9	29.6	58.5	35.8	29.2	57.9	34.9
10	33.3	−30.9	−6.0	34.6	−26.0	−2.0
11	15.7	97.0	24.2	14.7	96.6	19.0
12	20.4	−70.1	−3.9	20.2	−71.8	−5.0
13	86.4	20.1	7.4	88.4	21.9	9.5
14	32.4	−24.7	−11.4	35.0	−15.4	−3.1
15	37.5	20.8	3.7	36.5	18.6	1.1
16	26.0	−13.1	9.2	25.1	−17.1	6.0

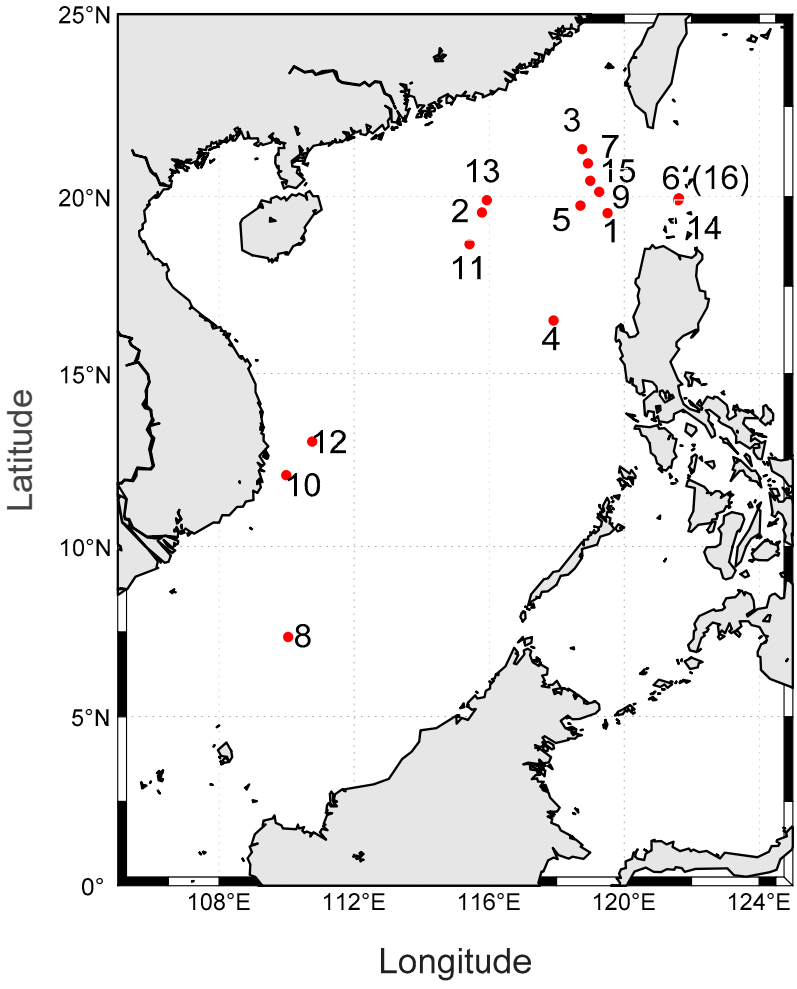

Figure 5. The map of the coordinates of the selected points. (Number 6 and 16 are located at the same position).

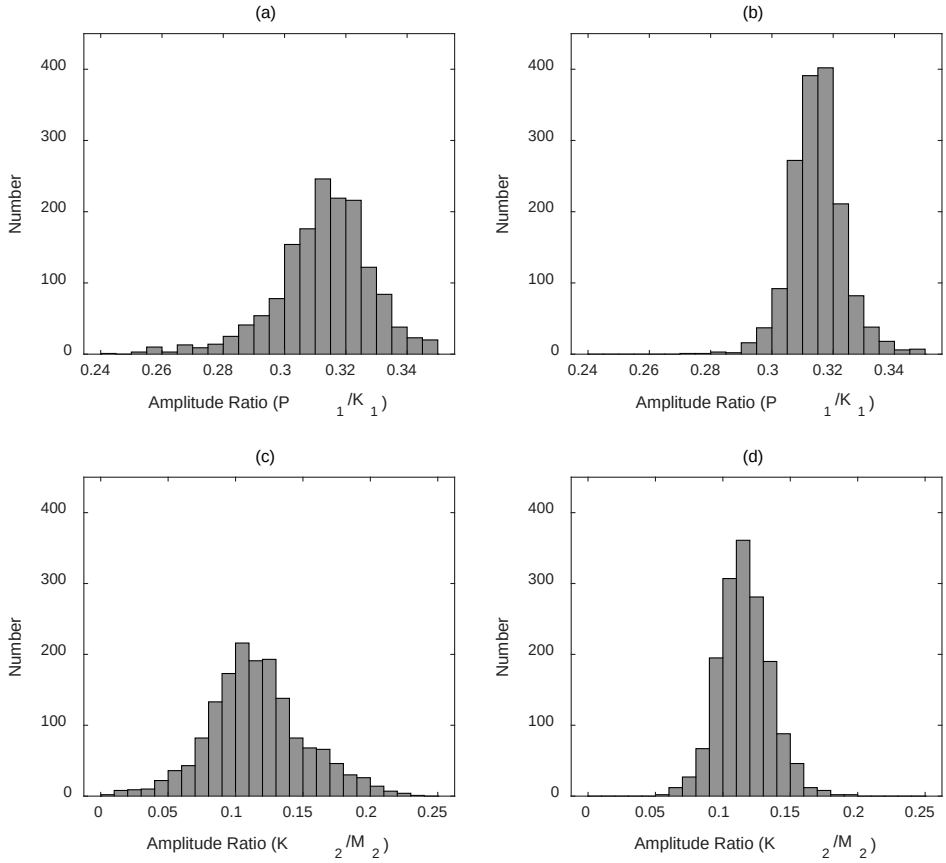

Figure 6. Histogram of the ratio of the P_1 tidal amplitude to the K_1 amplitude and the ratio of the K_2 tidal amplitude to the M_2 amplitude in the South China Sea: (**a**) P_1/K_1 before the MVC; (**b**) P_1/K_1 after the MVC; (**c**) K_2/M_2 before the MVC; (**d**) K_2/M_2 after the MVC.

Through the above verifications, after MVC, the influence of MOV on altimeter-based tidal estimates is thought to have been successfully removed, and thus, the results are extremely close to the actual values.

3.2. The Effect of MVC on the Estimation of Tidal Phase

Figure 7 and Table 7 show the results of tidal phase difference (Δg) before and after MVC; detailed distribution statistics are displayed in Table A2 in Appendix A. The MOV has a distinct influence on the estimation of tidal phases of distinct constituents. The phases of M_2 and O_1 are the least affected by MOV, whose phase differences are mainly distributed within ±3°. The M_2 (O_1) tide has a maximum phase difference of 8.56° (2.95°) and the minimum is −3.51° (−2.36°). The distribution of the phase differences of the K_2 tide is relatively dispersed, ranging from −176.27° to 86.46°, and most of these values are negative. Similar to the amplitude, the influence of MOV on the phase of K_2 tides in the SCS is also much greater than that of other major constituents.

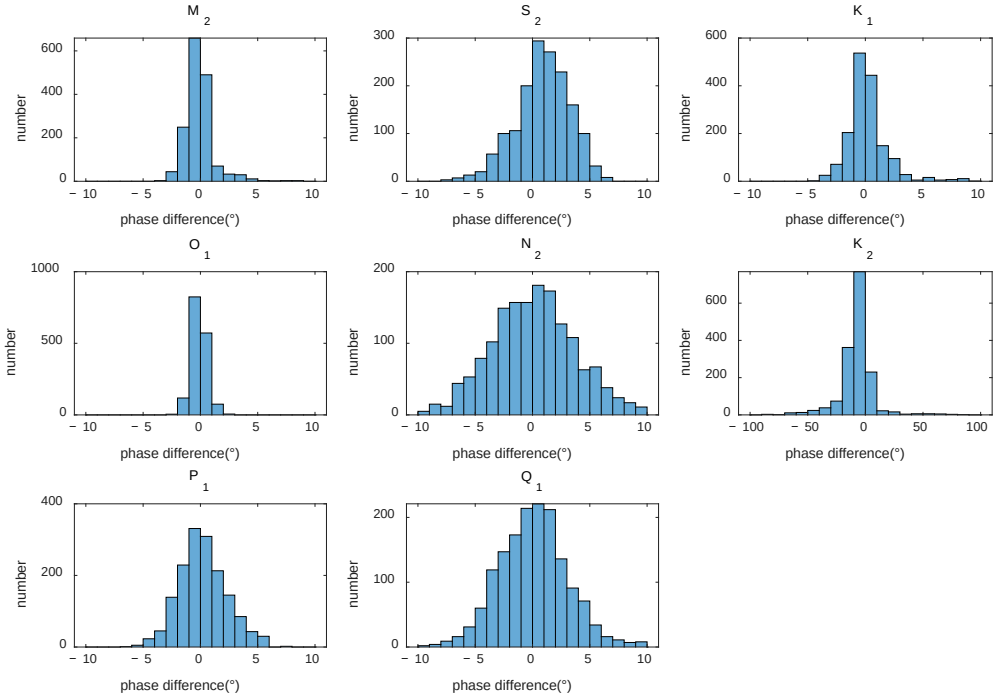

Figure 7. Histogram of the phase difference before and after MVC of the eight tides in the South China Sea.

Table 7. Extreme values of the phase difference (PD) before and after MVC of the eight major constituents in the South China Sea.

Constituent	M_2	S_2	K_1	O_1	N_2	K_2	P_1	Q_1
Maximum PD (°)	8.56	6.98	9.19	2.95	15.02	86.46	7.68	13.85
Minimum PD (°)	−3.51	−7.85	−4.37	−2.36	−10.77	−176.27	−6.07	−15.52

3.3. Spatial Influence of Mesoscale Variability on Tidal Estimation

Figure 8 shows the spatial distribution of amplitude differences and phase differences before and after MVC of M_2 and O_1 tides in the SCS, respectively. The influence of MOV on altimeter-based tidal estimation is distinct in space. For these two tidal constituents, the common point is that the amplitude and phase differences increase significantly in the west of Luzon Strait (the extreme value appears at 20.68°N, 119.03°E). In addition, at the western boundary of the deep-ocean basin, the amplitude difference of M_2 clearly increases, whereas the amplitude difference of O_1 significantly decreases (the extreme value appears at 11.46°N and 111.36°E). Compared with the areas with high mesoscale eddy activities in the SCS mentioned above, we find that there is a certain overlap, which indicates that the altimeter-based tidal estimation is more vulnerable to the background noise when the mesoscale variability is strong.

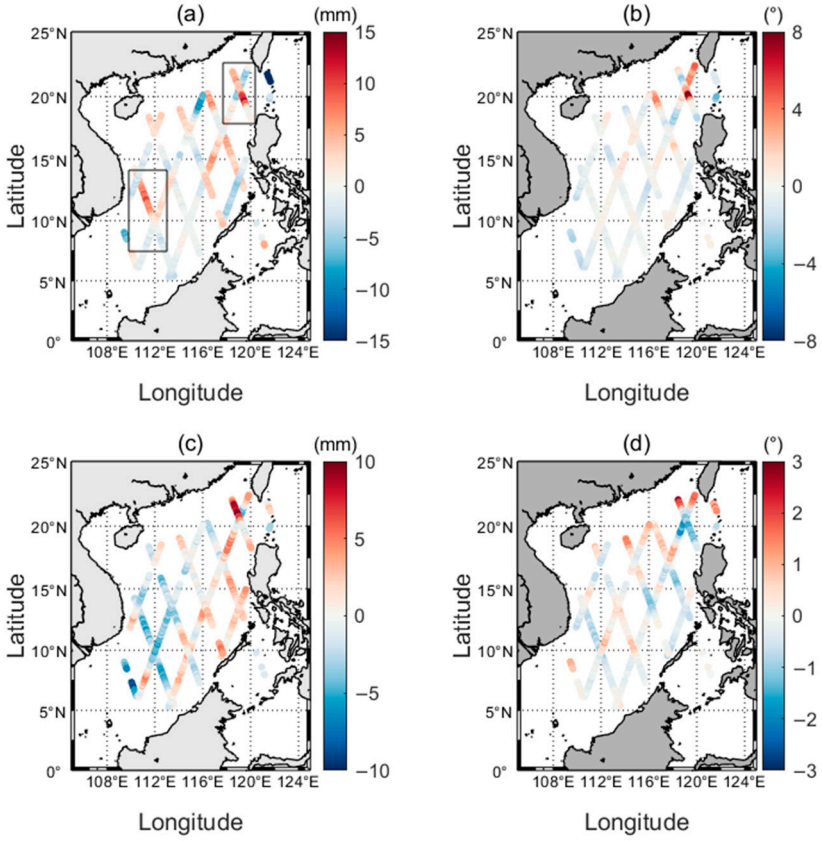

Figure 8. Spatial distribution of M_2 and O_1 tidal amplitude differences and phase differences before and after the MVC in the South China Sea: (**a**) the amplitude differences of M_2 (the west of Luzon Strait and the western boundary of the deep ocean basin are marked in the map); (**b**) the phase differences of M_2; (**c**) the amplitude differences of O_1; (**d**) the phase differences of O_1.

4. Discussion

4.1. Influence of Mesoscale Variability on the Estimation of Tidal Evolution

In recent years, sea level rise related to global warming and human activities such as land reclamation have significantly altered the water depth and coastline, which further influences the propagation of tidal waves [37–39]. Numerous studies have shown that tidal amplitudes are not stationary in many regions around the world [40–42]. Flick et al. (2003) found that the tidal range in San Francisco increased by 64 mm from 1900 to 1998, whereas in Wilmington, N.C., tidal range was found to have increased by 542 mm per century from 1935 to 1999 using the National Oceanic and Atmospheric Administration (NOAA) long-term tide gauge data [43]. In 1990, Woodworth noted that the tidal range of 13 ports in the British Isles had trends ranging from −1.8 to 1.3 mm [44]. In 2010, he further noted that long-term tidal changes are common around the world based on quasi-global tide gauge observations [45]. In the past few decades, the research of tidal evolution has been conducted by analyzing tide gauge data, and few studies have been conducted using satellite altimeter data. Although sea level observations at tide gauges are long, they are limited to coastal areas. By contrast, satellite altimeter observations are wider in space, and have been accumulated for more than 20 years. Although it is feasible to study tidal evolution using satellite data, but the interference of MOV remains uncertain.

To explore the tidal evolution, we divided the T/P-Jason observations into two periods, which were bounded on 1 January 2005. Tidal harmonic analysis during the two periods was carried out on the T/P-Jason data before and after the correction ($H_{1992\sim2005}$ and $H_{2005\sim2017}$ are the amplitudes before correction, $H'_{1992\sim2005}$ and $H'_{2005\sim2017}$ are the amplitudes after correction), and the amplitude differences between the two periods were compared ($H_{2005\sim2017} - H_{1992\sim2005}$, $H'_{2005\sim2017} - H'_{1992\sim2005}$). Comparing the tidal ampli-

tude changes before and after the MVC offers a glimpse of the effect of mesoscale variability on altimeter-based tidal evolution. Here, only the results of the four major tides, namely, M_2, S_2, K_1, and O_1 are shown in Figures 9 and 10. It can be seen that the evolution of tidal amplitudes of the four constituents in some areas is abnormally significant before MVC. These abnormally large values are eliminated after MAC, which indicates that they are not real but induced by MOV.

By comparing the tidal evolution before and after the MVC, we conclude that there are a large number of artificial changes in the tidal evolution caused by MOV (Figure 11). Mesoscale variability significantly increases the number of spatial points with large temporal changes of tidal amplitude. In addition, the extreme values of the tidal changes in the SCS increase. For example, in the case of the K_1 tide, when the MOV is uncorrected, the maximum amplitude change of K_1 is 52.7 mm, and the minimum is −32.3 mm. After the MVC, the maximum and minimum amplitudes change sharply, decreasing to 23.2 and −11.0 mm, respectively (Table 8). The mesoscale variability has a significant influence on the tidal evolution results. In some specific areas, the influence is large and the results without MVC cannot be trusted.

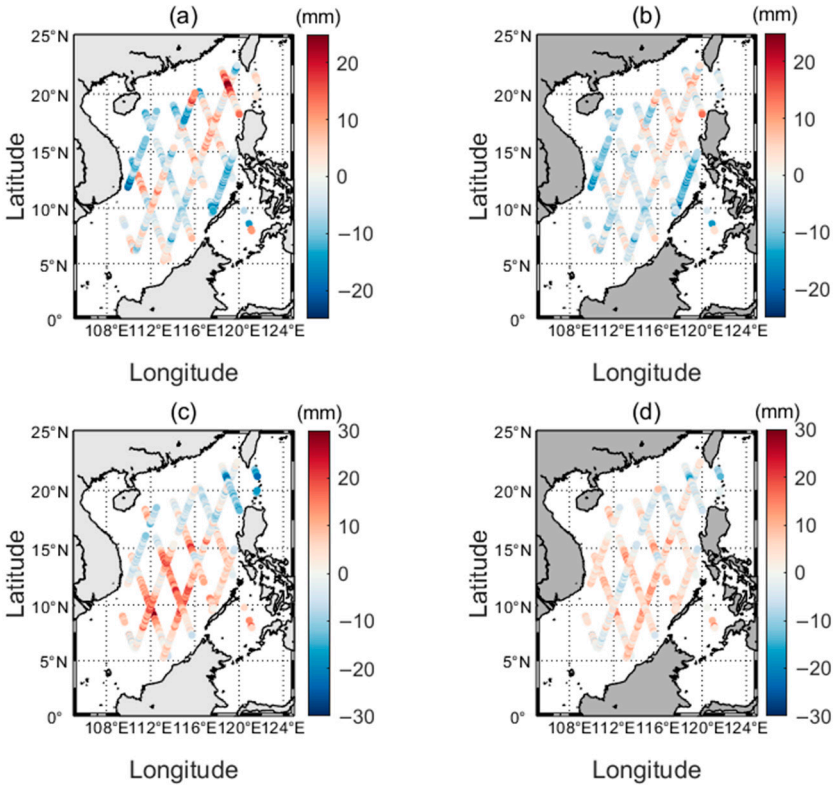

Figure 9. Comparison of the evolution of M_2 and S_2 tidal amplitudes before and after the MVC: (**a**) evolution of M_2 tidal amplitudes before correction; (**b**) evolution of M_2 tidal amplitudes after correction; (**c**) evolution of S_2 tidal amplitudes before correction; (**d**) evolution of S_2 tidal amplitudes after correction.

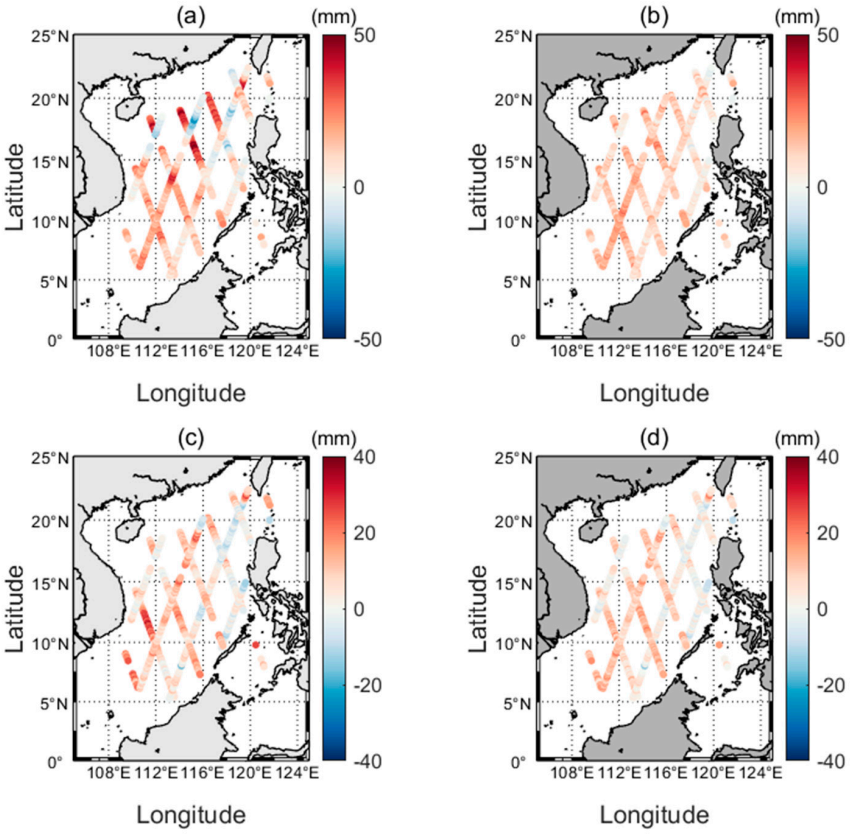

Figure 10. Comparison of evolution of K_1 and O_1 tidal amplitudes before and after the MVC: (**a**) evolution of K_1 tidal amplitudes before correction; (**b**) evolution of K_1 tidal amplitudes after correction; (**c**) evolution of O_1 tidal amplitudes before correction; (**d**) evolution of O_1 tidal amplitudes after correction.

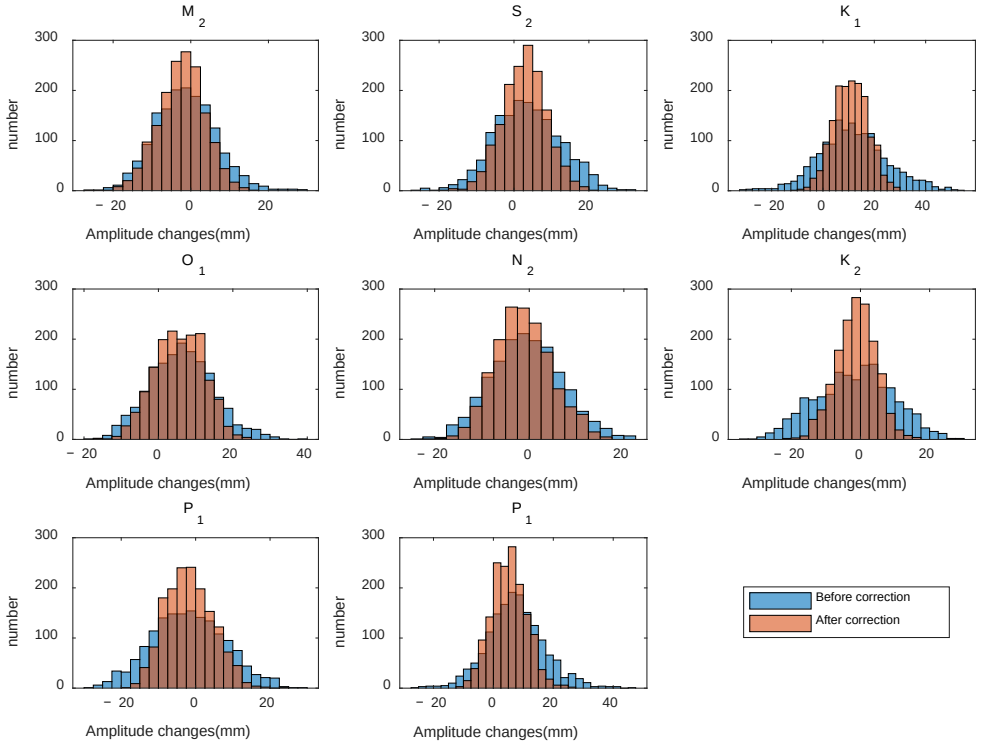

Figure 11. Histogram of amplitude change before and after the MVC based on T/P-Jason data.

Table 8. The extreme values of amplitude changes before and after the MVC of the eight major constituents in the South China Sea.

Constituent	Maximum (mm)			Minimum (mm)		
	Before Correction	After Correction	Difference	Before Correction	After Correction	Difference
$_M{}^2$	29.7	16.2	13.5	−26.7	−25.3	−1.4
S_2	32.5	21.2	11.3	−25.7	−17.8	−7.9
K_1	52.7	29.5	23.2	−32.3	−11.0	−21.3
O_1	39.1	24.9	14.2	−17.8	−15.6	−2.2
N_2	22.3	17.5	4.8	−23.9	−20.5	−3.4
K_2	28.6	17.0	11.6	−32.6	−21.7	−10.9
P_1	28.1	23.4	4.7	−27.6	−17.8	−9.8
Q_1	45.3	27.3	18	−25.7	−11.0	−14.7

4.2. Tidal Evolution in the South China Sea

The selected data points are distant from the coast and mainly located in the deep-sea basin in the central part of the SCS; the water depth in the central deep-sea basin of the SCS is more than 2000 m, with the maximum depth reaching 5500 m. Therefore, the change of water depth caused by sea level rise has a limited impact on the tidal changes in this region. Located in the tropical monsoon climate zone, the sea water in the SCS has strong stratification [46]. It should also be noted that the SCS is one of the most active regions of internal tides in the world [47–49]. The points at which the temporal changes of K_1 (O_1) tidal amplitude exceed 25 (18) mm are marked in Figure 12. It is clear that these points are mainly located in the areas where the bottom topography is complex and the water depth changes sharply in space, which is conducive to the generation of the internal tides. Baroclinic energy conversion is highly related to the ocean stratification, which has an obvious long-term trend in the SCS due to global warming. Therefore, we think it is likely that the evolution of surface tides in this region is induced by the changing ocean stratification under global warming via baroclinic generation. A similar phenomenon occurs at Hawaii, where internal tides are also strong. Colosi and Munk (2004) noted that the long-term trend of M_2 tidal amplitude in this area was related to the response of internal tidal phase to ocean warming by analyzing the observations of multi-year tide gauge data [50].

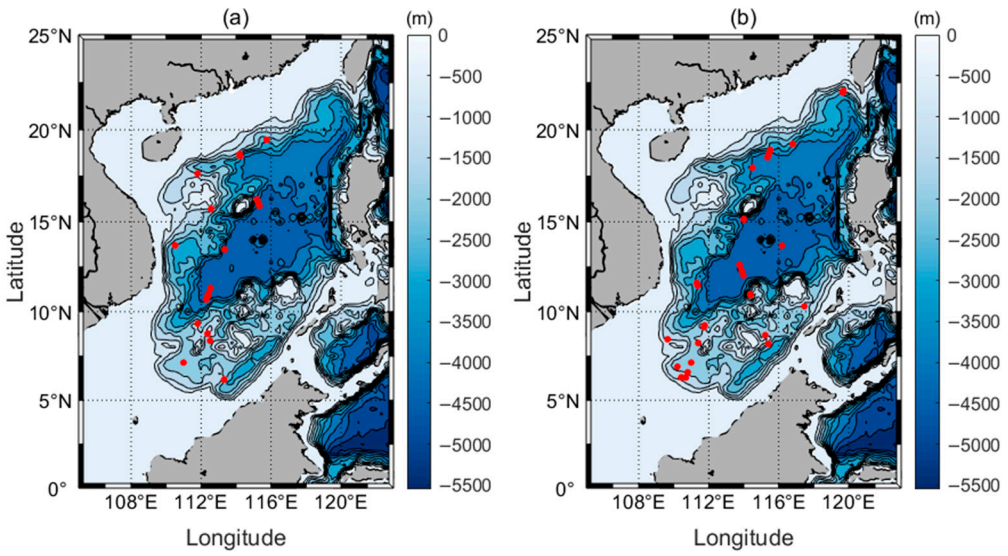

Figure 12. The water depth in the South China Sea and the point where (**a**) the temporal changes of amplitude in K_1 exceeds 25 mm (red in the figure); and (**b**) the tidal amplitude change in O_1 exceeds 18 mm (red in the figure).

5. Summary and Conclusions

The accurate extraction of tidal characteristics could be used to provide reliable predictions for future tides, which is important for coastal construction and shipping transportation. In addition, the demands for tidal information in the scientific community have become more exacting in recent years. This paper provides a reference for experiments that need high-quality tidal constants.

The harmonic constants based on T/P-Jason satellite observations are usually mixed with the contributions of non-tidal components, and particularly the MOV. This paper quantifies the influence of the MOV on the satellite-based results of tidal harmonic analysis in the SCS for the first time, using the SLA product to extract pure tidal field. The results show that the effects of the MOV on different tidal constituents are distinct. In terms of the absolute influence, the N_2 tide is less affected, and the absolute amplitude differences (AADs) of 64.81% of data points before and after the MVC are within ± 2 mm. In terms of the relative influence, the K_2 tide is the most affected by the MOV, mainly because the amplitude of the K_2 tide is less than 2 cm. The maximum and minimum AADs before and after the MVC account for 60.38% and -74.15% of the K_2 amplitude. As the largest tidal constituents in the SCS, the estimation of M2, K1, and O1 tides is not significantly influenced by the MOV.

For some areas with intense MOV in the SCS, particularly in the western part of the Luzon Strait, the south of the northern continental slope and the western boundary of the deep-sea basin, the tides are significantly disturbed by the MOV. It was also found that, in some regions, the rapid changes of tidal amplitudes are not genuine and are caused by the MOV. Therefore, the MVC must be performed in advance to obtain the real satellite-based tidal evolution.

Supplementary Materials: The S_TIDE toolbox used in this article can be obtained from the following website: https://www.researchgate.net/project/A-non-stationary-tidal-analysis-toolbox-S-TIDE.

Author Contributions: Conceptualization, H.P. and X.L.; Data curation, X.L. and H.P.; Formal analysis, Q.Y. and H.P.; Funding acquisition, Y.G. and X.L.; Investigation, Y.G. and X.L.; Methodology, Q.Y. and H.P.; Software, H.P.; Supervision, Y.G. and X.L.; Validation, Y.G. and X.L.; Writing—original draft, Q.Y.; Writing—review & editing, Q.Y., Y.G., H.P. and X.L. All authors have read and agreed to the published version of the manuscript.

Funding: This paper is supported by the National Natural Science Foundation of China (41706006, 42076011 and U1806214) and the National key research and development program (2019YFC1408405).

Data Availability Statement: The satellite altimeter data used in our study can be downloaded from the Radar Altimeter Database System (http://rads.tudelft.nl/rads/rads.shtml, last access: 1 May 2021). The filtered sea level anomaly (SLA) products can be obtained by request from Edward D. Zaron (Edward.D.Zaron@oregonstate.edu) or downloaded from the following website (https://drive.google.com/open?id=1cu3k_1Vjq_DdVGYvA5FRG70VXyUp_ngI, last access: 1 May 2021).

Conflicts of Interest: The authors declare no conflict of interest.

Appendix A

Table A1. Distribution of amplitude difference (AD) before and after the MVC of eight major tidal constituents in the South China Sea.

AD (mm)	<−10	−10~−6	−6~−2	−2~2	2~6	6~10	>10
M_2	12	45	293	743	413	82	12
S_2	0	2	432	843	287	36	0
K_1	44	175	397	569	277	88	50
O_1	2	19	419	791	342	26	1
N_2	0	13	312	1037	222	16	0
K_2	43	72	272	752	365	91	5
P_1	0	29	310	911	320	29	1
Q_1	0	43	336	814	391	16	0

Table A2. Distribution of phase difference (PD) before and after the MVC of eight major tidal constituents in the South China Sea.

PD (°)	−90~−20	−20~−9	−7~−9	−5~−7	−3~−5	−3~−1	−1~1	1~3	3~5	5~7	7~9	9~20	20~90
M_2	0	0	0	0	3	293	1149	103	41	5	6	0	0
S_2	0	0	3	20	77	206	494	500	260	40	0	0	0
K_1	0	0	0	0	27	275	981	244	33	21	18	1	0
O_1	0	0	0	0	0	123	1396	81	0	0	0	0	0
N_2	0	6	27	97	181	306	338	300	171	105	41	28	0
K_2	164	437	149	171	186	138	94	57	44	37	31	33	41
P_1	0	0	0	6	68	368	640	358	128	30	2	0	0
Q_1	0	9	13	47	179	320	435	348	162	50	18	19	0

References

1. Chao, B.F.; Ray, R.D. Oceanic Tidal Angular Momentum and Earth's Rotation Variations. *Prog. Oceanogr.* **1997**, *40*, 399–421. [CrossRef]
2. Munk, W.; Wunsch, C. The Moon, of Course. *Oceanography* **1997**, *10*, 132–134. [CrossRef]
3. Francis, O.; Mazzega, P. Global Charts of Ocean Tide Loading Effects. *J. Geophys. Res.* **1990**, *951*, 11411–11424. [CrossRef]
4. Desai, S.; Wahr, J.; Chao, Y. Error Analysis of Empirical Ocean Tide Models Estimated from TOPEX/POSEIDON Altimetry. *J. Geophys. Res.* **1997**, *102*, 25157–25172. [CrossRef]
5. Tierney, C.; Parke, M.; Born, G. An Investigation of Ocean Tides Derived from Along-Track Altimetry. *J. Geophys. Res.* **1998**, *103*, 10273–10287. [CrossRef]
6. Ray, R.; Byrne, D. Bottom Pressure Tides along a Line in the Southeast Atlantic Ocean and Comparisons with Satellite Altimetry. *Ocean Dyn.* **2010**, *60*, 1167–1176. [CrossRef]
7. Xiu, P.; Chai, F.; Shi, L.; Xue, H.; Chao, Y. A Census of Eddy Activities in the South China Sea during 1993–2007. *J. Geophys. Res. Ocean* **2010**, *115*. [CrossRef]
8. Dale, W.L. Wind and Drift Current in the South China Sea. *Malay. J. Trop. Geogr.* **1956**, *8*, 1–31.
9. Cheng, Y.-H.; Ho, C.-R.; Zheng, Q.; Qiu, B.; Hu, J.; Kuo, N.-J. Statistical Features of Eddies Approaching the Kuroshio East of Taiwan Island and Luzon Island. *J. Oceanogr.* **2017**, *73*, 427–438. [CrossRef]
10. Chen, G.; Hou, Y.; Chu, X. Mesoscale Eddies in the South China Sea: Mean Properties, Spatiotemporal Variability, and Impact on Thermohaline Structure. *J. Geophys. Res. Ocean* **2011**, *116*. [CrossRef]
11. Yanagi, T.; Morimoto, A.; Ichikawa, K. Co-Tidal and Co-Range Charts for the East China Sea and the Yellow Sea Derived from Satellite Altimetric Data. *J. Oceanogr.* **1997**, *53*, 303–309.
12. Yanagi, T.; Takao, T.; Morimoto, A. Co-Tidal and Co-Range Charts in the South China Sea Derived from Satellite Altimetry Data. *La Mer* **1997**, *35*, 85–93.
13. Fang, G.; Kwok, Y.; Yu, K.; Zhu, Y. Numerical Simulation of Principal Tidal Constituents in the South China Sea, Gulf of Tonkin and Gulf of Thailand. Cont. *Shelf Res.* **1999**, *19*, 845–869. [CrossRef]
14. Zu, T.; Gan, J.; Erofeeva, S.Y. Numerical Study of the Tide and Tidal Dynamics in the South China Sea. *Deep-Sea Res.* **2007**, *55*, 137–154. [CrossRef]
15. Pan, H.; Lv, X.; Wang, Y.; Matte, P.; Chen, H.; Jin, G. Exploration of Tidal-Fluvial Interaction in the Columbia River Estuary Using S_TIDE. *J. Geophys. Res.* **2018**, *123*, 6598–6619. [CrossRef]
16. Pascual, A.; Faugère, Y.; Larnicol, G.; Le Traon, P.Y. Improved Description of the Ocean Mesoscale Variability by Combining Four Satellite Altimeters. Geophys. *Res. Lett.* **2006**, *33*, 3–7. [CrossRef]
17. Zaron, E.; Ray, R. Aliased Tidal Variability in Mesoscale Sea Level Anomaly Maps. *J. Atmos. Ocean. Technol.* **2018**, *35*. [CrossRef] [PubMed]

18. Schlax, M.; Chelton, D. Aliased Tidal Errors in TOPEX/POSEIDON Sea Surface Height Data. *J. Geophys. Res. Atmos.* **1995**, *99*. [CrossRef]
19. Fang, G.; Wang, Y.; Wei, Z.; Choi, B.; Wang, X.; Wang, J. Empirical Cotidal Charts of the Bohai, Yellow, and East China Seas from 10 Years of TOPEX/Poseidon Altimetry. *J. Geophys. Res.* **2004**, *109*. [CrossRef]
20. Leffler, K.; Jay, D. Enhancing Tidal Harmonic Analysis: Robust (Hybrid L1/L2) Solutions. *Cont. Shelf Res.* **2009**, *29*, 78–88. [CrossRef]
21. Pan, H.; Zheng, Q.; Lv, X. Temporal Changes in the Response of the Nodal Modulation of the M2 Tide in the Gulf of Maine. *Cont. Shelf Res.* **2019**, *186*, 13–20. [CrossRef]
22. Pan, H.; Lv, X. Is There a Quasi 60-Year Oscillation in Global Tides? *Cont. Shelf Res.* **2021**, *222*, 104433. [CrossRef]
23. Pawlowicz, R.; Beardsley, B.; Lentz, S. Classical Tidal Harmonic Analysis with Error Analysis in MATLAB Using T_TIDE. *Comput. Geosci.* **2002**, *28*, 929–937. [CrossRef]
24. Anderson, K. Determination of Water Level and Tides Using Interferometric Observations of GPS Signals. *J. Atmos. Ocean. Technol.* **2000**, *17*, 1118–1127. [CrossRef]
25. Wang, G.; Su, J.; Chu, P. Mesoscale Eddies in the South China Sea Observed with Altimeter Data. *Geophys. Res. Lett.* **2003**, *30*. [CrossRef]
26. Li, J.; Zhang, R.; Jin, B. Eddy Characteristics in the Northern South China Sea as Inferred from Lagrangian Drifter Data. *Ocean Sci.* **2011**, *7*. [CrossRef]
27. Liu, C.; Du, Y.; Zhuang, W.; Xia, H.; Xie, Q. Evolution and Propagation of a Mesoscale Eddy in the Northern South China Sea during Winter. *Acta Oceanol. Sin.* **2013**, *32*. [CrossRef]
28. Zhang, M.; Von Storch, H.; Chen, X.; Wang, D.; Li, D. Temporal and Spatial Statistics of Travelling Eddy Variability in the South China Sea. *Ocean Dyn.* **2019**, *69*. [CrossRef]
29. Egbert, G.; Bennett, A.F.; Foreman, M. TOPEX/POSEIDON Tides Estimated Using a Global Inverse Model. *J. Geophys. Res.* **1994**, *99*, 821–852. [CrossRef]
30. Egbert, G.; Erofeeva, S. Efficient Inverse Modeling of Barotropic Ocean Tides. *J. Atmos. Ocean. Technol.* **2002**, *19*, 183–204. [CrossRef]
31. Lyard, F.H.; Allain, D.J.; Cancet, M.; Carrère, L.; Picot, N. FES2014 Global Ocean Tide Atlas: Design and Performance. *Ocean Sci.* **2021**, *17*, 615–649. [CrossRef]
32. Cartwright, D.; Ray, R. Oceanic Tides from Geosat Alimetry. J. Geophys. *Res. Atmos.* **1990**, *95*. [CrossRef]
33. Godin, G. *The Analysis of Tides*; University of Toronto Press: Toronto, ON, Canada, 1972; p. 264.
34. Parker, B. *Tidal analysis and prediction. NOAA Special Publ. NOS CO-OPS 3*; National Oceanic and Atmospheric Administration: Washington, DC, USA, 2007; p. 378.
35. Pugh, D.; Woodworth, P. *Sea-Level Science: Understanding Tides, Surges, Tsunamis and Mean Sea-Level Changes*; Cambridge University Press: Cambridge, UK, 2012; p. 395.
36. Ray, R.D. On Tidal Inference in the Diurnal Band. *J. Atmos. Ocean. Technol.* **2017**, *34*, 437–446. [CrossRef]
37. Müller, M. Rapid Change in Semi-Diurnal Tides in the North Atlantic since 1980. *Geophys. Res. Lett.* **2011**, *38*. [CrossRef]
38. Rodrıguez-Padilla, I.; Ortiz, M. On the Secular Changes in the Tidal Constituents in San Francisco Bay. *J. Geophys. Res. Ocean.* **2017**, *122*, 7395–7406. [CrossRef]
39. Devlin, A.; Jay, D.; Zaron, E.; Talke, S.A.; Pan, J.; Lin, H. Tidal Variability Related to Sea Level Variability in the Pacific Ocean. *J. Geophys. Res. Ocean.* **2017**. [CrossRef]
40. Ray, R.D. Secular Changes of the M2 Tide in the Gulf of Maine. *Cont. Shelf Res.* **2006**, *26*, 422–427. [CrossRef]
41. Müller, M.; Arbic, B.K.; Mitrovica, J.X. Secular Trends in Ocean Tides: Observations and Model Results. *J. Geophys. Res. Ocean.* **2011**, *116*, 1–19. [CrossRef]
42. Ku, L.; Greenberg, D.; Garrett, C.; Dobson, F. Nodal Modulation of the Lunar Semidiurnal Tide in the Bay of Fundy and Gulf of Maine. *Science* **1985**, *230*, 69–71. [CrossRef]
43. Flick, R.E.; Murray, J.F.; Ewing, L.C.; Asce, M. Trends in United States Tidal Datum Statistics and Tide Range. *J. Waterw. Port Coast. Ocean Eng.* **2003**, *129*, 155–164. [CrossRef]
44. Woodworth, P.L.; Shaw, S.M.; Blackman, D.L. Secular Trends in Mean Tidal Range around the British Isles and along the Adjacent European Coastline. *Geophys. J. Int.* **1991**, *104*, 593–609. [CrossRef]
45. Woodworth, P. A Survey of Recent Changes in the Main Components of the Ocean Tide. *Cont. Shelf Res.* **2010**, *30*, 1680–1691. [CrossRef]
46. Colosi, J.; Munk, W. Tales of the Venerable Honolulu Tide Gauge*. *J. Phys. Oceanogr.* **2006**, *36*. [CrossRef]
47. Guo, P.; Fang, W.; Liu, C.; Qiu, F. Seasonal Characteristics of Internal Tides on the Continental Shelf in the Northern South China Sea. *J. Geophys. Res.* **2012**, *117*, 4023. [CrossRef]
48. Alford, M.; MacKinnon, J.; Nash, J.; Simmons, H.; Pickering, A.; Klymak, J.; Pinkel, R.; Sun, O.; Rainville, L.; Musgrave, R.; et al. Energy Flux and Dissipation in Luzon Strait: Two Tales of Two Ridges. *J. Phys. Oceanogr.* **2011**, *41*, 2211–2222. [CrossRef]
49. Jan, S.; Chern, C.S.; Wang, J.; Chao, S.Y. Generation of Diurnal K1internal Tide in the Luzon Strait and Its Influence on Surface Tide in the South China Sea. *J. Geophys. Res.* **2007**, *112*. [CrossRef]
50. Alford, M.; Peacock, T.; Mackinnon, J.; Nash, J.; Buijsman, M.; Centuroni, L.; Chao, S.-Y.; Chang, M.-H.; Farmer, D.; Fringer, O.; et al. The Formation and Fate of Internal Waves in the South China Sea. *Nature* **2015**, *521*, 65–69. [CrossRef]